THE JOURNAL OF PHYSICAL CHEMISTRY LETTERS
A JOURNAL OF THE AMERICAN CHEMICAL SOCIETY

pubs.acs.org/JPCL Letter

Unveiling the Redox Noninnocence of Metallocorroles: Exploring K-Edge X-ray Absorption Near-Edge Spectroscopy with a Multiconfigurational Wave Function Approach

Rishu Khurana and Cong Liu*

Cite This: https://doi.org/10.1021/acs.jpclett.4c02410 Read Online

ACCESS | Metrics & More | Article Recommendations | Supporting Information

ABSTRACT: X-ray absorption near-edge spectroscopy (XANES) is an advanced technique for probing the local electronic structure of catalysts, effectively identifying the noninnocent nature of ligands in transition-metal complexes. Metallocorroles with noninnocent corrole rings exhibit unusual electronic structures that challenge traditional density functional theory (DFT) methods, necessitating more rigorous approaches to describe electron correlation accurately. We explored K-edge XANES spectra of Fe, Mn, and Co metallocorroles using TDDFT and wave function-based methods. This is the first investigation employing multireference methods, specifically RASSCF, RASPT2, and MC-PDFT, to analyze the redox noninnocent nature of metallocorroles reflected in their XANES spectra. We quantified the noninnocent character of the corrole and the oxidation states of the metals, capturing more than singly excited excitations responsible for the pre-edge peak. Our findings demonstrate the importance of these advanced computational techniques for accurately predicting XANES spectra, providing a reliable understanding of the electronic properties of such complexes. This study offers a new strategy for investigating ligand redox noninnocence via integrated experimental and computational XANES.

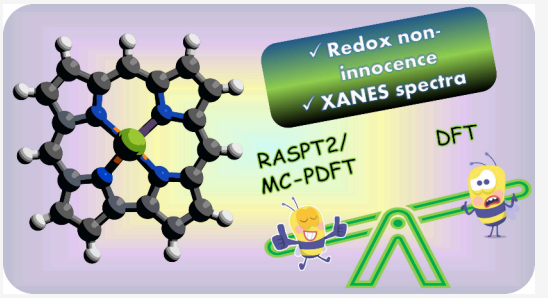

X-ray absorption near-edge spectroscopy (XANES) has emerged as a potent tool for delving into the local electronic and structural properties of catalyst molecules and materials.[1,2] XANES contains valuable information about the oxidation state, coordination environment, and the local symmetry of the metal centers in the catalysts.[3−5] In particular, in the K-edge XANES of 3d-transition metal catalysts, the rising edge manifests a 1s → 4p transition that is used to estimate the charge on the metal center, metal−ligand overlap via shakedown transitions, and geometric structure. However, various factors, such as spin state, multiple scattering, metal−ligand distances, etc., influence the position of the rising edge. The pre-edge region that emerges as the result of electric dipole-forbidden but quadrupole-allowed 1s → 3d transition offers a distinctive means to investigate the electronic and geometric structure, such as 3d vacant orbitals and thus the spin state and the oxidation state of the metal.[6,7] However, the subtle features obtained in the XANES spectra are difficult to rationalize based on solely the experimental XANES. Therefore, through computational simulation of XANES spectra coupled with molecular orbital analysis, a more in-depth understanding of the underlying electronic interactions between the metal center and its coordination environment can be obtained.[8,9] The integration of computational and experimental XANES proves to be a resilient approach, providing a detailed analysis that facilitates thorough characterization of structural features of a material. XANES stands as a robust technique to identify ligand noninnocence within transition-metal complexes.[10−13] Redox noninnocent ligands due to their unique electronic structure provide an opportunity to modify their reactivity and catalytic properties.[14−17] Metallocorroles are the archetypal illustrations of ligands exhibiting a noninnocent nature, where the macrocyclic ring exhibits partial corrole$^{\bullet 2-}$ character.[18,19] These compounds have garnered attention due to their promising applications in catalysis.[20−23] Ghosh et al. has used XAS to explore the noninnocent behavior of metallocorroles within the families of manganese, iron, cobalt, copper, and silver.[24−28]

Various computational methods are available to calculate the core−valence excitations, such as delta self-consistent field approach (ΔSCF),[29] multiple scattering method,[30] time-dependent density functional theory (TDDFT),[31−38] and wave function-based coupled-cluster methods.[39,40] Among all of the methods, TDDFT is extensively employed in modeling XANES ascribed to its balanced combination of accuracy and computational cost. However, TDDFT tends to underestimate the core−valence excitation energy and thus requires a

Received: August 16, 2024
Revised: October 10, 2024
Accepted: October 22, 2024

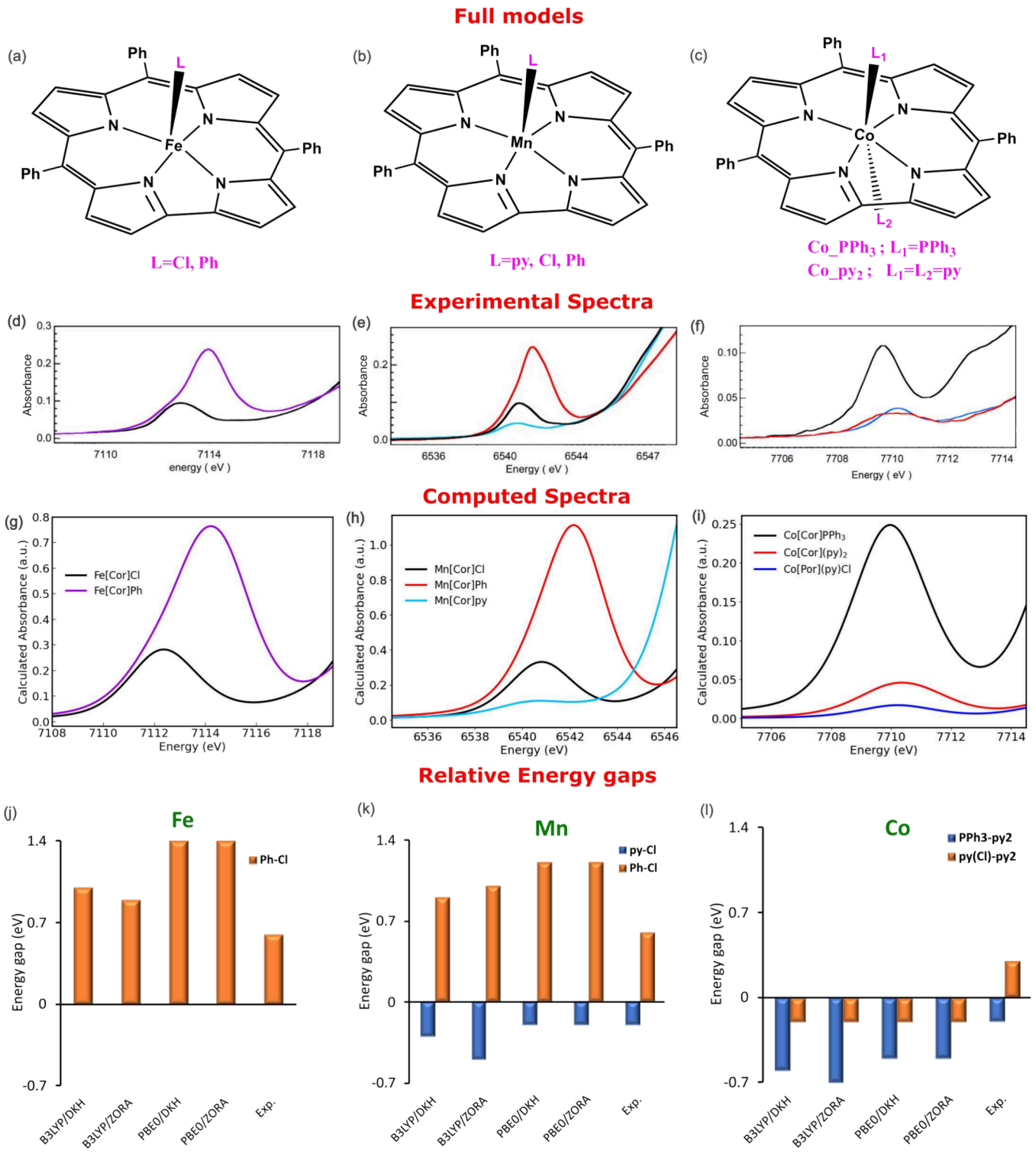

Figure 1. Structures of metallocorroles of (a) Fe, (b) Mn, and (c) Co under study. The structure of metalloporphyrin, i.e., Co[Por](py)Cl, is presented in Figure S1. Experimental spectra of (d) Fe, (e) Mn, and (f) Co complexes taken from refs 24−26. Computed spectra of (g) Fe, (h) Mn, and (i) Co complexes obtained from TDDFT at PBE0/DKH/DKH-DEF2-TZVP level. The spectra for Fe, Mn, and Co complexes are energy-shifted by 83, 80.7, and 86 eV, respectively, in order to compare with the experimental spectra. The comparison of relative energy gap (in eV) among different complexes from different functionals and basis sets and experimental values of (j) Fe, (k) Mn, and (l) Co complexes. The energy gaps are calculated as the difference of IWAE energies of two complexes. The pre-edge energies of Fe[Cor]Cl, Mn[Cor]Cl, and Co[Cor](py)$_2$ are set as reference (0 eV) in panels j, k, and h, respectively. The experimental data are reproduced from refs 24−26 with copyright permission and are modified.

rigorous calibration, like linear-shift correction, to acquire quantitative accuracy with experimental results.[31,34,35,41] Additionally, achieving quantitative accuracy in TDDFT simulations of XANES relies on selecting appropriate functionals and basis sets and incorporating relativistic effects.[31] Moreover, for transition-metal complexes with near-degenerate electronic

https://doi.org/10.1021/acs.jpclett.4c02410
J. Phys. Chem. Lett. XXXX, XXX, XXX−XXX

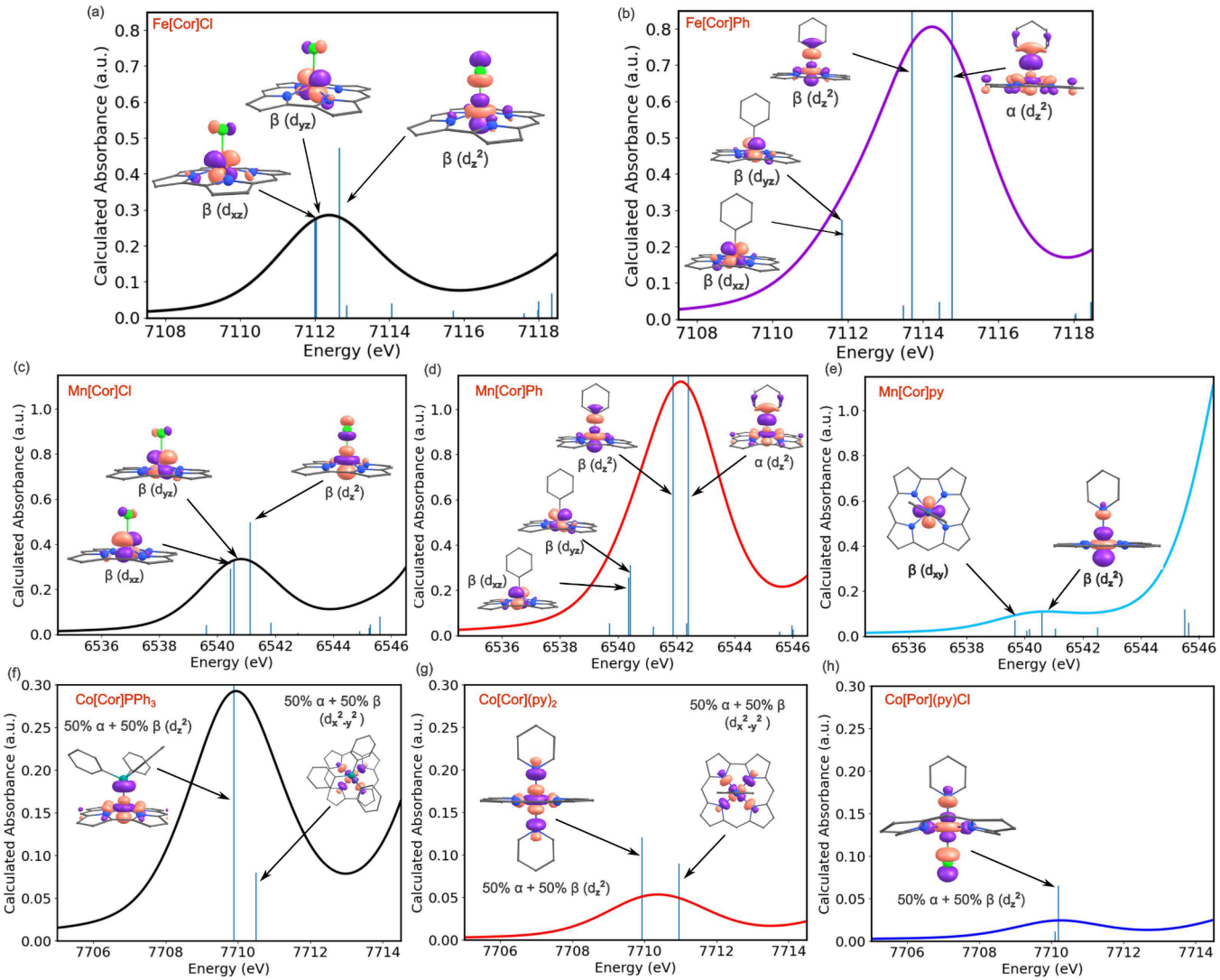

Figure 2. Analysis of individual transition responsible for TDDFT pre-edge spectra of (a) Fe[Cor]Cl, (b) Fe[Cor]Ph, (c) Mn[Cor]Cl, (d) Mn[Cor]Ph, (e) Mn[Cor]py, (f) Co[Cor]PPh_3, (g) Co[Cor]$(py)_2$, and (h) Co[Por](py)Cl obtained at PBE0/DKH/DKH-DEF2-TZVP level. The spectra for Fe, Mn, and Co complexes are energy-shifted by 83, 80.7, and 86 eV, respectively, in order to compare with the experimental spectra.

states, it misses excitations that involve higher-order configurations and fails to correctly account for the multiplet effects. Multireference wave function methods like multi-reference configuration interaction (MRCI)[42,43] or multi-reference coupled cluster (MRCC)[44] can effectively capture higher-order configurations with sufficient accuracy. Nonetheless, their computational cost becomes prohibitive for systems beyond a few atoms. The restricted active space self-consistent field (RASSCF), a wave function-based method, excels as an efficient approach that offers an accurate description of the wave function for multireference systems.[45] Further, to account for the dynamical correlations, second-order perturbation theory, i.e., RASPT2, is usually employed.[46] Guo et al. have employed RASSCF/RASPT2 calculations to obtain the iron K pre-edge X-ray absorption spectra for open-shell iron complexes.[47] Govind and co-workers recently used multi-configuration pair-density functional theory (MC-PDFT)[48] to characterize the metal K pre-edge features of aquated 3d-transition metal ions, showing performance comparable to RASPT2 but with significantly lower computational cost.[49,50]

Metallocorroles exhibit unusual electronic structures that challenge traditional single-reference DFT methods and thus require more rigorous methods that provide a more reliable description of electron correlation. Roos et al. have studied the electronic structure of chloroiron corrole using CASSCF/CASPT2 supporting S = 3/2 Fe(III) antiferromagnetically coupled with a corrole radical.[51] Phung et al. studied the electronic structure and quantified the noninnocent character of different 3d and 4d metallocorroles employing DMRG/CASPT2.[52,53] Despite the significance of multireference methods in elucidating the electronic structure of metallocorroles, a comprehensive ab initio computational study of XANES for these compounds using multireference techniques remains conspicuously absent. This study seeks to fill this gap by examining the XANES spectra of the Fe, Mn, and Co metallocorroles. We conducted a comparative analysis between XANES simulations generated through DFT and multi-reference methods (RASSCF/RASPT2/MC-PDFT), contrasting them with the available experimental XANES data. Our findings underscore the significance of employing wave function-based methods for accurate electronic structure

https://doi.org/10.1021/acs.jpclett.4c02410
J. Phys. Chem. Lett. XXXX, XXX, XXX−XXX

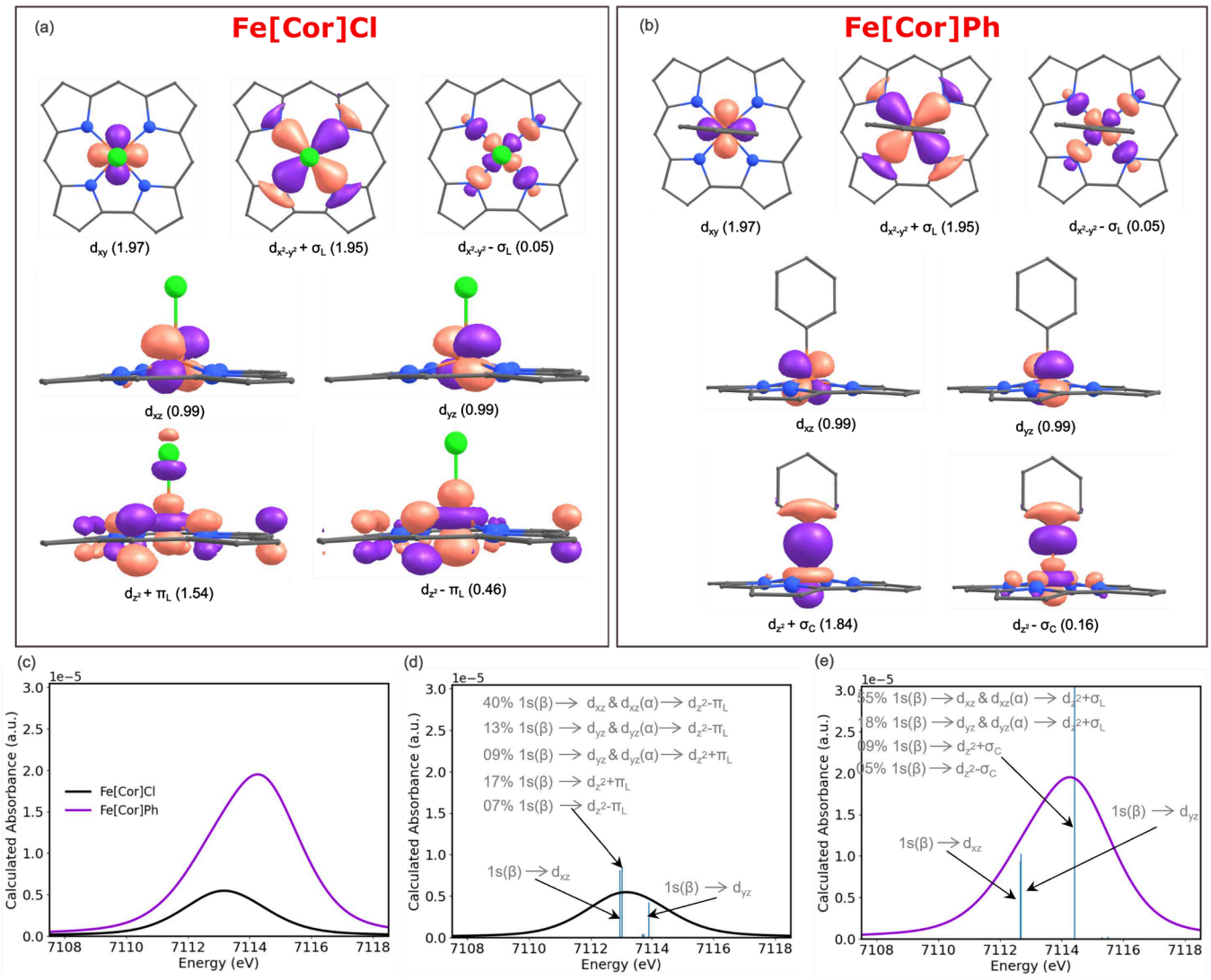

Figure 3. Active orbitals of (a) Fe[Cor]Cl and (b) Fe[Cor]Ph obtained in RAS2 subspace after converged RASSCF calculations. The 4d orbitals obtained in RAS2 are not shown. (c) Computed XANES spectra obtained from MC-PDFT. The analysis of individual transitions responsible for pre-edge XANES peak for (d) Fe[Cor]Cl and (e) Fe[Cor]Ph complexes. The spectra are energy-shifted by −9 eV in order to compare with the experimental spectra.

calculations and XANES predictions of such complexes. Intriguingly, we identified the reflection of the ligand redox noninnocence in the metal K pre-edge XANES region.

The Fe-substituted tris(phenyl) corroles, denoted as Fe-[TPC]X (where X = Cl, Ph); Mn-tris(*p*-CF_3-phenyl) corroles, Mn[T*p*CF_3PC]X (X = Cl, Ph, py); and Co-tris(phenyl) corroles, Co[TPC]X (X = PPh_3, $(py)_2$), are illustrated in Figure 1a−c, and Co-tetrakis(phenyl) porphyrin, Co[TPP]Cl-(py), is shown in Figure S1. The K pre-edge XANES spectra calculated for these substituted metallocorroles employing TDDFT (PBE0/DKH/DKH-DEF2-TZVP/AUTOAUX) are shown in Figure 1g−i. The relative intensities between the different complexes in the spectra from the calculations correlate well with experimental data (Figure 1d−f).[24−26]

To simplify the models for further calculations, we removed the phenyl groups from the corrole ligands (Figure S2). Spectral comparisons between the original and simplified models (Figure S2) indicate that phenyl substitutions minimally impact the pre-edge peaks, validating the use of these simplified models for further studies. Initially, we determined the pre-edge energies of unsubstituted complexes using B3LYP and PBE0 functionals, paired with DKH and ZORA relativistic corrections (Table S1). For B3LYP/DKH, a linear shift of 87−93 eV was needed to match experimental energies, decreasing to 16−32 eV with B3LYP/ZORA. With PBE0, shifts were further reduced to 80−86 eV with DKH and 10−25 eV with ZORA corrections. Thus, PBE0/ZORA/ZORA-def2-TZVP is optimal for closely matching experimental peak energies with minimal shifts. Similar energy shifts with the incorporation of different Hamiltonians have been observed in previous studies.[41,54] Nevertheless, notable deviations emerge between the intensity-weighted average energy (IWAE) peak derived from TDDFT calculations and the corresponding experimental peaks, as observed in the relative energies among different complexes from different TDDFT functionals and experimental energies (Figure 1j,i). The experimental energy difference between Fe[Cor]Cl and Fe[Cor]Ph peaks is 0.6 eV, increasing to 1.4 eV with the PBE0 functional. The energy gap between Mn[Cor]py and Mn[Cor]Cl is 0.2 eV, aligning with the experimental data. However, the

https://doi.org/10.1021/acs.jpclett.4c02410
J. Phys. Chem. Lett. XXXX, XXX, XXX−XXX

Table 1. Electronic Configuration of the Ground State for Fe[Cor]Cl and Fe[Cor]Ph[a]

			Electronic configuration							
Complex	No.	% cont.	1s	d_{xy}	$d_{x^2-y^2} + \sigma_L$	$d_{x^2-y^2} - \sigma_L$	d_{xz}	d_{yz}	$d_{z^2} + \pi_L/\sigma_C$[b]	$d_{z^2} - \pi_L/\sigma_C$[b]
Fe[Cor]Cl	1	66	2	2	2	0	u	u	2	0
	2	14	2	2	2	0	u	u	0	2
	3	07	2	2	2	0	u	u	d	u
	4	04	2	2	2	0	u	u	u	d
Fe[Cor]Ph	1	86	2	2	2	0	u	u	2	0
	2	06	2	2	2	0	u	u	0	2

[a]u and d mean α and β electron, respectively. [b]π_L is for Fe[Cor]Cl and σ_C is for Fe[Cor]Ph.

gap between Mn[Cor]Ph and Mn[Cor]Cl is 1.2 eV, twice the experimental value (0.6 eV). A notable divergence arises in the DFT-predicted energy trends for Co complexes. This can be observed in Figure 1i where the energy gap between Co[Por](py)Cl and Co[Cor](py)$_2$ is positive from experiments; however, it is negative from all the DFT methods. Despite these discrepancies, the computed relative peak intensities remain in good agreement with experimental observations.

Further, we examined the individual transitions associated with the pre-edge spectra and the natural transition orbitals (NTOs) corresponding to the most intense transitions (Figure 2). For Fe[Cor]Cl (Figure 2a), three dominant transitions are primarily responsible for the pre-edge peak. The first two transitions overlap with each other and correspond to β electron transitioning from 1s to $3d_{xz}$ and $3d_{yz}$ orbitals. The third transition, being most intense, involves a β electron moving from 1s → $3d_{z^2}$. Figure 2b illustrates individual transitions for Fe[Cor]Ph, featuring four major transitions. The first two overlapping transitions involve the excitation of β electron from 1s to $3d_{xz}$ and $3d_{yz}$. The third and fourth transitions, which are more intense, involve excitation of both 1s β and α electrons to $3d_{z^2}$, respectively. Mn[Cor]Cl and Mn[Cor]Ph exhibit similar transitions as that of Fe analogues, with Ph being higher in intensity than Cl (Figure 2c,d). For Mn[Cor]py, the pre-edge features two peaks of nearly equal intensity, but the overall pre-edge intensity is very low. One involves the transfer of the 1s β electron to $3d_{xy}$, and the other corresponds to $3d_{z^2}$ (Figure 2e). For Co[Cor]PPh$_3$, two dominant transitions are majorly responsible for the pre-edge energy peak. Both of them involve transition of 50% α and 50% β 1s electron to $3d_{z^2}$ and 3 $d_{x^2-y^2}$, respectively (Figure 2f). The same orbitals are involved in the transition for Co[Cor](py)$_2$; however, the intensity of the first transition is much smaller compared to the PPh$_3$ analogue (Figure 2g). The Co[Por](py)Cl involves the transition of 50% α and 50% β 1s electron to $3d_{z^2}$ (Figure 2h).

The electronic structure of these metallocorroles has been already studied by DFT, so we will refrain from the discussion of the electronic structure from DFT. Fe[TPC]Cl is supported to contain the noninnocent corrole$^{2-\bullet}$ antiferromagnetically coupled to $S = 3/2$ Fe (III) center by magnetic susceptibility measurements and DFT calculations.[55] Similarly, Fe[TPC]Ph has been characterized using various spectroscopic techniques, X-ray crystallography, and DFT calculations, revealing a low-spin iron species coordinated to a closed-shell corrolate trianion and a phenyl monoanion.[56] DFT spin-density suggests a mix of Fe(IV) and Fe(III) oxidation states as

$$Fe^{IV}(\uparrow\uparrow) - Ph \leftrightarrow Fe^{III}(\uparrow\uparrow\uparrow) - Ph^{\bullet}(\downarrow) \quad (1)$$

However, determining the exact balance between different oxidation states of iron requires more advanced multi-configurational calculations beyond traditional DFT.

Therefore, we analyzed the electronic structure of the metallocorroles using multireference calculations. Further, we examined the XANES spectra and pre-edge peak energies derived from these multireference approaches. The active orbitals with average occupancies from RASSCF for Fe[Cor]Cl and Fe[Cor]Ph are illustrated in Figure 3a and b. The orbital pairs $d_{x^2-y^2} + \sigma_L$ and $d_{x^2-y^2} - \sigma_L$ describe the modest interaction of σ orbitals of nitrogen atoms in corrole (σ_L) with $d_{x^2-y^2}$ of the metal center in both cases. However, the d_{z^2} orbital interacts strongly with corrole's π orbitals (π_L) in the case of Fe[Cor]Cl, resulting in a linear combination of $d_{z^2} + \pi_L$ and $d_{z^2} - \pi_L$ orbitals. This interaction gives rise to radical character on the corrole ring. No such interaction is present in Fe[Cor]Ph, but in this case, the σ orbital of the phenyl ring (σ_C) interacts with d_{z^2} of the metal. This substantiates the innocent nature of the corrole ring in Fe[Cor]Ph.

The ground state of Fe[Cor]Cl comprises four electronic configurations (Table 1). In each configuration, the electron occupancy varies between $d_{z^2} + \pi_L$ and $d_{z^2} - \pi_L$. The dominant configuration with a 66% contribution features two electrons in $d_{z^2} + \pi_L$ with $d_{z^2} - \pi_L$ being unoccupied. The second configuration (14%) has electrons present in $d_{z^2} - \pi_L$ and $d_{z^2} + \pi_L$ remains vacant. The remaining configurations, contributing 7% and 4%, have one electron with spin-up and one with spin-down distributed across these two orbitals. To quantify the radical character, we computed the effective bond order (EBO) using the equation[57]

$$EBO = \frac{NOON_{bonding} - NOON_{antibonding}}{2} \quad (2)$$

Here NOON refers to natural orbital occupation numbers for bonding and antibonding orbitals. The percentage of radical character (%rad) is determined by

$$\%rad = (1 - EBO) \times 100 \quad (3)$$

Using the average NOONs shown in Figure 3a, considering the occupation number of $d_{z^2} + \pi_L$ as $NOON_{bonding}$ and $d_{z^2} - \pi_L$ as $NOON_{antibonding}$, the %rad character is calculated to be 46%. This indicates that the corrole ring in Fe[Cor]Cl possesses significant radical character of 46%, underscoring the noninnocent behavior of the corrole in this complex.

For Fe[Cor]Ph, the ground state primarily consists of one major configuration with 86% contribution where the two electrons reside in $d_{z^2} + \sigma_C$ in the major contribution while $d_{z^2} - \sigma_C$ remains unoccupied and vice versa for the minor configuration (6%) (Table 1). Although the corrole ligand acts

https://doi.org/10.1021/acs.jpclett.4c02410
J. Phys. Chem. Lett. XXXX, XXX, XXX−XXX

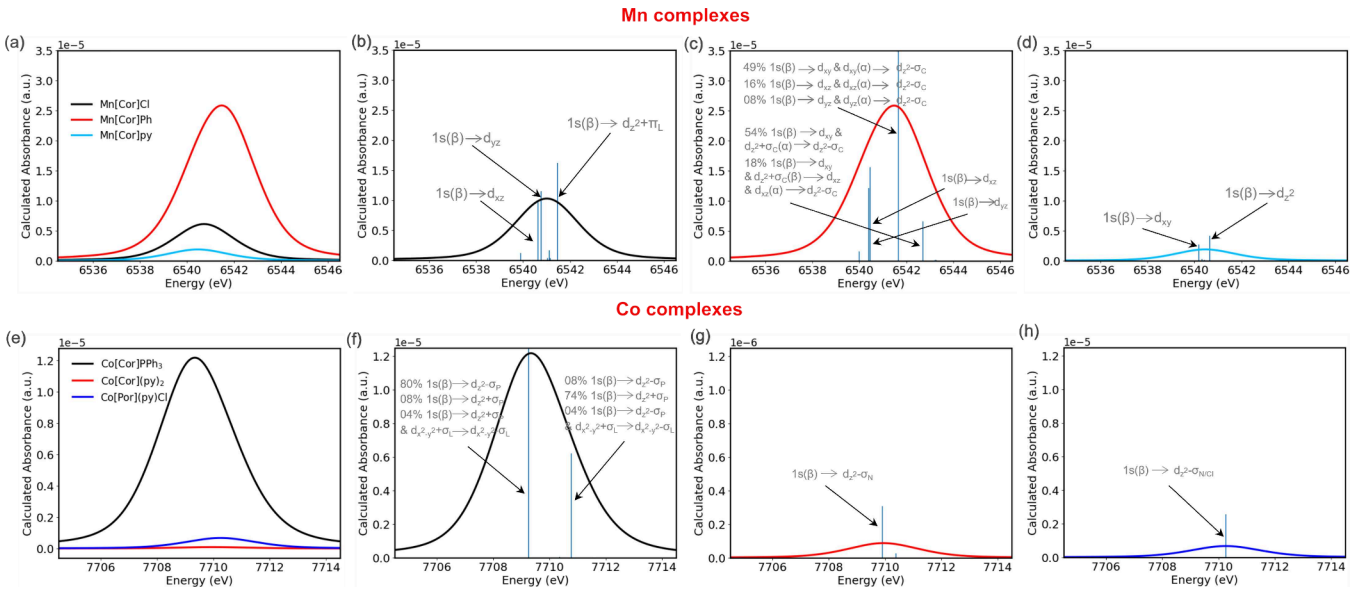

Figure 4. Computed XANES spectra obtained from MC-PDFT for (a) Mn and (e) Co metallocorroles. The analysis of individual transitions responsible for pre-edge XANES peak for (b) Mn[Cor]Cl, (c) Mn[Cor]Ph, (d) Mn[Cor]py, (f) Co[Cor]PPh_3, (g) Co[Cor]$(py)_2$, and (h) Co[Por](py)Cl. The spectra are energy-shifted by −6.5 and −10.7 eV for Mn and Co complexes, respectively, in order to compare with the experimental spectra.

as innocent within this complex, electron transfer between Fe and Ph is evident, as described by eq 1. Thus, we analyzed the extent of this electron transfer to the Ph ring using eqs 2 and 3. Considering the occupancy of $d_{z^2} + \sigma_C$ as $NOON_{bonding}$ and $d_{z^2} - \sigma_C$ as $NOON_{antibonding}$ resulted in 84% electron on $d_{z^2} + \sigma_C$ and 16% electron on $d_{z^2} - \sigma_C$. This distribution suggests the electron localization is primarily on the Ph ring, with a portion allocated to Fe. Consequently, the oxidation state of Fe is predominantly Fe(IV), with a possible composition of 84% Fe(IV) and 16% Fe(III). This exemplifies the capability of multiconfigurational methods to quantify the percentage of the metal's oxidation state. This also highlights the importance of using multireference methods in metallocorroles and justifies their use in computing XANES spectra.

Further, we computed XANES spectra of Fe metallocorroles using RASSCF, RASPT2, and MC-PDFT methods. The MC-PDFT-computed XANES spectra are plotted in Figure 3c. The relative peak intensities align well with the experimental observations. For Fe[Cor]Cl, three primary transitions are responsible for pre-edge peak (Figure 3d and Table S2). The first excited state (ES1) comprises three configurations, each involving a β electron transitioning from 1s to $3d_{xz}$ orbital. In ES2 with three configurations, each configuration involves excitation of the β electron from 1s to $3d_{yz}$ orbital. The ES3 has significant contribution from five different configurations. The first configuration with 40% contribution is obtained by transfer of the 1s β electron to $3d_{xz}$ and then the transfer of the α electron in $3d_{xz}$ to $3d_{z^2} - \pi_L$. The second configuration (13%) is obtained by excitation of the 1s β electron to $3d_{yz}$ and then the transfer of the α electron in $3d_{yz}$ to $3d_{z^2} - \pi_L$. The fourth transition (9%) involves the transfer of 1s β electron to $3d_{yz}$ and subsequent transfer of the α electron from $3d_{yz}$ to $3d_{z^2} + \pi_L$. These three transitions involve higher than singly excited configurations, which are challenging to obtain from TDDFT and are not observed. The third (17%) and fifth (7%) transitions are single electron excitation involving direct transfer of the 1s β electron to $3d_{z^2} + \pi_L$ and $3d_{z^2} - \pi_L$, respectively. In contrast, TDDFT predicted it as the single excitation of the 1s β electron directly to the $3d_{z^2}$. For Fe[Cor]Ph, there are three dominant transitions responsible for the pre-edge energy peak (Figure 3e and Table S3). The ES1 is primarily dominated by one electronic configuration with 79% contribution where the β 1s electron excites to $3d_{xz}$. The second configuration (7%) also involves the transfer of the β 1s electron to $3d_{xz}$. The ES2 involves excitation of the β 1s electron to $3d_{yz}$. The ES3 consists of four distinct contributions and is notably the most intense. The first, with 55% contribution, includes transition of the β 1s electron to $3d_{xz}$, followed by movement of the α $3d_{xz}$ electron to $3d_{z^2} + \sigma_C$. The second transition (18%) involves the β 1s electron moving to $3d_{yz}$ and the α $3d_{yz}$ electron proceeding to $3d_{z^2} + \sigma_C$. These transitions are characterized as involving more complex configurations than merely singly excited states and are not captured by DFT. The remaining two transitions include a direct shift of the 1s β electron to $3d_{z^2} + \sigma_C$ and $3d_{z^2} - \sigma_C$, respectively.

The active orbitals with their average occupancies for Mn and Co metallocorroles are shown in Figures S3 and S4. The ground state of Mn[Cor]Cl comprises four different electronic configurations (Table S4). Each configuration differs in the occupancy of $d_{z^2} + \pi_L$ and $d_{z^2} - \pi_L$. The dominant configuration (51%) has two electrons in the $d_{z^2} + \pi_L$. The configuration with 18% contribution has two electrons in the $d_{z^2} - \pi_L$. The remaining two configurations have one α and one β in the two orbitals. The radical character, as calculated using eqs 2 and 3, is determined to be 60%, which is higher than the 46% radical character in Fe[Cor]Cl. This result closely aligns with the findings of Phung et al., who reported 45% and 61% radical character in Fe[Cor]Cl and Mn[Cor]Cl, respectively, at the DMRG-CASSCF level.[52] Further, for Mn[Cor]Ph, the ground state consists of one major contribution with 84% contribution with two electrons present in $d_{z^2} + \sigma_C$ and another configuration with 6% contribution where $d_{z^2} - \sigma_C$ is occupied with two electrons (Table S5). We quantified the extent of electron transfer from the Ph ring to the Mn using eqs 2 and 3. It results in a combination of 80%

https://doi.org/10.1021/acs.jpclett.4c02410
J. Phys. Chem. Lett. XXXX, XXX, XXX−XXX

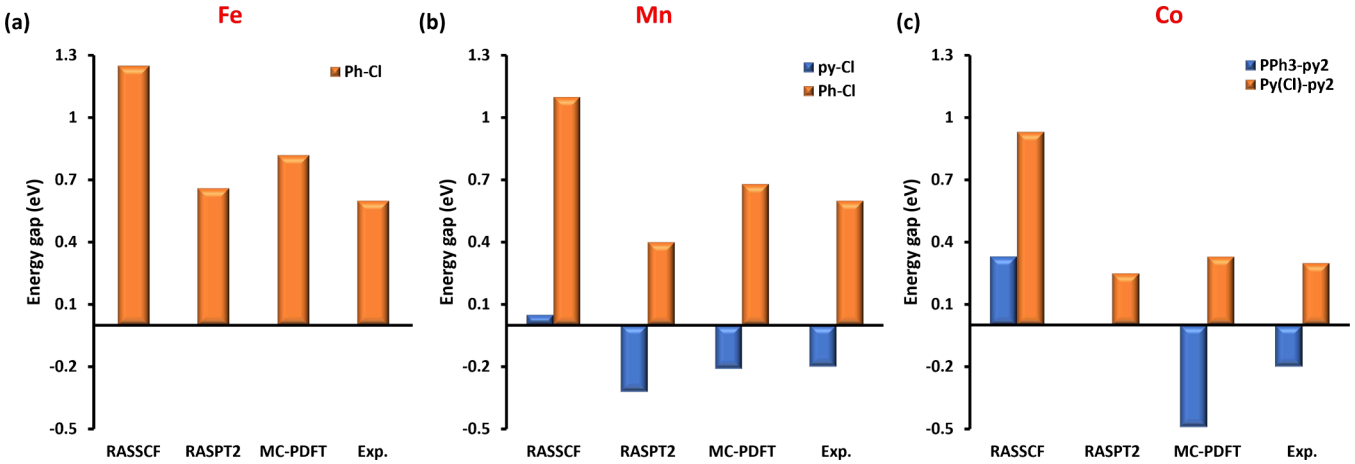

Figure 5. Comparison of relative energy gaps (in eV) among different complexes with different multireference methods for (a) Fe, (b) Mn, and (c) Co complexes. The energy gaps are calculated as the difference of IWAE energies of two complexes. The pre-edge energies of Fe[Cor]Cl, Mn[Cor]Cl, and Co[Cor](py)$_2$ are set as reference (0 eV) in panels a, b, and c, respectively.

Mn(IV) and 20% Mn(III) oxidation state in the complex. Mn[Cor]py is a single determinant system with a 97% electronic configuration (Table S6). Further, the XANES spectra plotted from MC-PDFT for all of the Mn metallocorroles are shown in Figure 4a. A closer look at the individual transitions for Mn[Cor]Cl revealed that there are three significant transitions (Figure 4b). The first one involves the transfer of the 1s β electron to 3d$_{xz}$. The second and third transitions are obtained by transfer of β electron from 1s to 3d$_{yz}$ and 3d$_{z^2}$ + π_L, respectively (Table S4). For Mn[Cor]Ph, there are four major transitions (Figure 4c). The first two transitions involve the transfer of electron from 1s β to 3d$_{xz}$ and 3d$_{yz}$, respectively. The third transition involves the transfer of 1s β electron to 3d$_{xy}$, 3d$_{xz}$, or 3d$_{yz}$ orbitals, with a simultaneous transfer of α electron from these orbitals to the 3d$_{z^2}$ − σ_C orbital. In the fourth transition, 54% involves the transfer of the 1s β electron to the 3d$_{xy}$ orbital, with a simultaneous transfer of the α electron from 3d$_{z^2}$ + σ_C to 3d$_{z^2}$ − σ_C. Additionally, 18% involves the transfer of a 1s β electron to 3d$_{xy}$, a β electron from 3d$_{z^2}$ + σ_C to 3d$_{xz}$, and an α electron from 3d$_{xz}$ to 3d$_{z^2}$ − σ_C. The last two transitions involve multiple excitations and are not captured by DFT, which depicts them as a single excitation of a β and α electron to 3d$_{z^2}$ (Table S5). For Mn[Cor]py, both DFT and multireference calculations predict the same transitions, involving the transfer of the 1s β electron to 3d$_{xy}$ and 3d$_{z^2}$ orbitals (Figure 4d and Table S6). For Co metallocorroles, the ground state of all the complexes primarily consists of one electronic configuration with 90% contribution, where d$_{x^2-y^2}$ − σ_L and d$_{z^2}$ − $\sigma_{P/N/Cl}$ orbitals (P for PPh$_3$, N for (py)$_2$, and N/Cl for (py)Cl ligands) are unoccupied, while the other orbitals are doubly occupied (Tables S7−S9). For Co[Cor]PPh$_3$, a minor contribution of 2% involves the occupancy of d$_{z^2}$ − σ_P with unoccupied d$_{z^2}$ + σ_P. The XANES spectra (Figure 4e) show good agreement between the intensity of the peaks in the experimental and computed spectra. Analysis of the individual contributions to the pre-edge peak shows two major transitions in Co[Cor]-PPh$_3$ (Figure 4f). The ES1 involves the transition of 80% of the 1s β electron to 3d$_{z^2}$ − σ_P and 8% to 3d$_{z^2}$ + σ_P. A small contribution of 4% involves 1s β electron transferring to 3d$_{z^2}$ + σ_P, with a simultaneous movement of a β electron from 3 d$_{x^2-y^2}$ + σ_L to 3 d$_{x^2-y^2}$ − σ_L. The ES2 is the reverse of first, with a major contribution of 74% due to transition of 1s β electron to 3d$_{z^2}$ + σ_P and 8% to 3d$_{z^2}$ − σ_P. A small contribution of 4% involves 1s β electron transferring to 3d$_{z^2}$ − σ_P, with a simultaneous movement of a β electron from 3 d$_{x^2-y^2}$ + σ_L to 3 d$_{x^2-y^2}$ − σ_L (Table S7). For Co[Cor](py)$_2$ and Co[Por](py)-Cl, there is only one transition in the spectra, corresponding to the transfer of the 1s β electron to 3d$_{z^2}$ − σ_N with 92% contribution for Co[Cor](py)$_2$ and to 3d$_{z^2}$ − $\sigma_{N/Cl}$ with 87% contribution for Co[Por](py)Cl. DFT predicts these transitions as 50% α and 50% β transition to 3d$_{z^2}$ and 3 d$_{x^2-y^2}$ for Co[Cor](py)$_2$, and 50% α and 50% β transition to 3d$_{z^2}$ for Co[Por](py)Cl, but transitions of this nature are not observed in multireference calculations (Tables S8 and S9).

The calculated pre-edge IWAE peaks for all cases are listed in Table S10. While the absolute peak energy values are not particularly informative, the relative energies of the computed pre-edge peaks across different complexes offer a practical way to evaluate the accuracy of the XANES simulations. Thus, we plotted the relative energy differences between the computed pre-edge energies for the three metallocorroles in Figure 5 and compared them with the experimental relative energy differences. The relative energy difference between the computed pre-edge energies for Fe[Cor]Cl and Fe[Cor]Ph from RASSCF is 1.25 eV, which is larger than the experimentally observed difference of 0.6 eV (Figure 5a). Additionally, the RASSCF energy trend for Mn and Co corroles does not align with the experimental data (Figure 5b,c). Specifically, the relative energy differences between Mn[Cor]py and Mn[Cor]-Cl, as well as between Co[Cor]PPh$_3$ and Co[Cor](py)$_2$, are negative in the experimental data but positive in the RASSCF results. Thus, static correlations alone are insufficient for accurately computing the XANES spectra.

Therefore, we incorporated dynamical correlations using two different methods: RASPT2 and MC-PDFT. Including dynamical correlations narrowed the energy difference between the peaks corresponding to the Fe metallocorroles to 0.66 and 0.82 eV with RASPT2 and MC-PDFT, respectively, highlighting the significance of incorporating dynamical correlations for achieving values closer to the experimental value of 0.6 eV. For Mn and Co complexes, the inclusion of dynamical correlations led to the correct energy trend, with the negative energy differences between the Mn[Cor]py and Mn[cor]Cl

https://doi.org/10.1021/acs.jpclett.4c02410
J. Phys. Chem. Lett. XXXX, XXX, XXX−XXX

and Co[Cor]PPh_3 and Co[Cor]$(py)_2$ in agreement with experimental trends. Precisely, for Mn[Cor]py and Mn[Cor]Cl with an experimental energy gap of 0.2 eV, MC-PDFT provided a good agreement with an energy gap of 0.21 eV and RASPT2 showed a slightly larger energy gap of 0.32 eV. The energy gap between Mn[Cor]Cl and Mn[Cor]Ph is 0.6 eV in experiments with MC-PDFT providing a 0.68 eV gap, which is in good agreement with the experimental value, and RASPT2 lowered the energy gap to 0.41 eV. For Co complexes, RASPT2 calculations were not performed on Co[Cor]PPh_3 due to high computational demands. However, MC-PDFT correctly predicted the energy trends for Co[Cor]PPh_3 and Co[Cor]$(py)_2$ although the energy gap (0.49 eV) is slightly higher than the experimentally observed gap (0.2 eV). The energy difference between Co[Por](py)Cl and Co[Cor]$(py)_2$ is in quite good agreement with the experimental value of 0.3 eV, with RASPT2 (0.25) and MC-PDFT (0.33 eV) showing similar gaps. Thus, MC-PDFT provides accurate energy gaps comparable to RASPT2 at a significantly lower computational cost. It is important to note that only multireference calculations, when complemented by dynamical correlations, accurately capture the trends for these complexes. This observation is in line with the findings of Polly et al. and Sergentu et al., who demonstrated the relative importance of orbital relaxation through CAS/RAS methods and the inclusion of dynamic correlation via second-order perturbation theory (PT2) for accurately predicting spectra.[58,59] Both DFT and static multireference calculations alone fail to do so. This underscores the critical role of incorporating dynamic correlations in multireference calculations for predicting such systems. Furthermore, it has been noted that TDDFT requires positive linear shifts to align with experimental spectra, whereas multireference calculations necessitate negative shifts (Tables S1 and S10). Specifically, MC-PDFT exhibits a smaller shift (−6 to −10 eV) compared to those of RASPT2 (−15 to −21 eV) and RASSCF (−17 to −22 eV). Ghosh et al. recently observed similar trends in their study of the K-edge XANES spectra of hexacoordinated aquated 3d-transition metal ions. The contrasting shift requirements might stem from inherent errors in TDDFT's nonvariational approach and potential self-interaction in the exchange−correlation functional, leading to positive shifts. In contrast, MC-PDFT and RASPT2 employ variational optimization of excited-state wave functions within the active space with frozen core orbitals to prevent variational collapse, hence requiring negative shifts. However, the freezing of core orbitals and limitations of the active space may impact the full relaxation of core-hole states, introducing additional approximations in the multireference approaches. Additionally, the smaller negative shift observed in MC-PDFT compared to RASPT2 is likely attributed to MC-PDFT's ability to account for correlation from all types of excitations, whereas RASPT2 primarily captures correlation from double excitations.[49]

In summary, a comprehensive study of the K-edge XANES spectra of the metallocorroles of Fe, Mn, and Co employing TDDFT and wave function-based RASSCF/RASPT2/MC-PDFT methods is undertaken. TDDFT struggles to accurately capture the percentage of noninnocent character of the ligand and fails to account for transitions involving more than a singly excited configuration. In contrast, wave function-based methods prove to be highly effective. MC-PDFT, a promising alternative to RASPT2 with only marginal computational cost, provides accurate predictions of the K-edge XANES spectra of noninnocent metallocorrole complexes. These methods excel in providing precise percentages of radical character and the oxidation states of the metal and effectively handle cases involving more than one single excited configuration. This pioneering study is the first to examine the XANES spectra of noninnocent metallocorroles using multireference methods, underscoring the significance of these advanced computational tools for investigating similar complexes. The groundbreaking insights gained from this research are poised to guide future XANES calculations for analogous systems, offering a deeper understanding of the electronic intricacies of the metallocorroles.

COMPUTATIONAL METHODS

All the structures are optimized at the B3LYP/def2-TZVP/AUTOAUX/RIJCOSX level.[60−63] TDDFT calculations are performed at four different levels: B3LYP/DKH/DKH-DEF2-TZVP/AUTOAUX/RIJCOSX, B3LYP/ZORA/ZORA-DEF2-TZVP/AUTOAUX/RIJCOSX, PBE0/DKH/DKH-DEF2-TZVP/AUTOAUX/RIJCOSX, and PBE0/ZORA/ZORA-DEF2-TZVP/AUTOAUX/RIJCOSX[60,64,65] with 50 excited states, incorporating Tamm-Dancoff approximation (TDA) and allowing for quadrupole contributions. The K-edge XAS spectra are obtained by designating the metal's 1s orbital as the donor orbital and any unoccupied orbital as the acceptor orbital. All DFT and TDDFT calculations are performed in Orca v5.0.4.[66] All RASSCF,[45] RASPT2,[46] MC-PDFT,[48] and RASSI[67] calculations are performed in OpenMolcas v23.10.[68] In multireference calculations, the careful selection of the active space, considering core, valence, and potentially noninnocent ligand orbitals, is key to achieving accurate and reliable electronic structure predictions. In RASSCF calculations for metal K pre-edge XANES calculation, the RAS1 subspace consists of the 1s orbital of the metal. The RAS2 subspace contains the five metals' 3d orbitals, two ligand-based orbitals, and three metals' 4d-orbitals. For Mn[Cor]py, only one ligand-based orbital is considered, while the other active space remains the same. The ground state is optimized separately, and ten excited states are considered for the core-excited-state calculations and are optimized in the state-average formalism. Only one hole is allowed in the RAS1 space during the core excited-state calculations. To ensure the excitation of electrons happens from 1s orbitals, the orbital was kept frozen during the RASSCF optimization. The RASSI approach is used to obtain spin−orbit coupled states using the DKH Hamiltonian and to calculate electric dipole oscillator strengths between the ground and excited states. Given that the complexes under study lack centrosymmetry and, thus, have large 3d−4p mixing, the electric dipole contributions are sufficient to effectively capture the K pre-edge features (since quadrupole-only transitions are only 1% of dipole-only transition).[24] ANO-RCC-VTZP is assigned on Fe, Mn, Co, N, Cl, and P, and ANO-RCC-VDZP is assigned on C and H[69] with DKH corrections. For RASPT2 calculations, an imaginary shift of 5.4 eV is employed without applying any IPEA shift. For MC-PDFT calculations, the tPBE on-top pair-density functional is employed.

ASSOCIATED CONTENT

Supporting Information

The Supporting Information is available free of charge at https://pubs.acs.org/doi/10.1021/acs.jpclett.4c02410.

https://doi.org/10.1021/acs.jpclett.4c02410
J. Phys. Chem. Lett. XXXX, XXX, XXX−XXX

Structures of simplified models, computed pre-edge peak energies with TDDFT and multireference calculations, RASSCF active orbitals, electronic configuration of different complexes from multireference calculations, details for XANES spectra (PDF)

xyz coordinate files (ZIP)

Transparent Peer Review report available (PDF)

AUTHOR INFORMATION

Corresponding Author

Cong Liu − *Chemical Sciences and Engineering Division, Argonne National Laboratory, Lemont, Illinois 60439, United States;* orcid.org/0000-0002-2145-5034; Email: congliu@anl.gov

Author

Rishu Khurana − *Department of Chemistry, The University of Chicago, Chicago, Illinois 60637, United States; Chemical Sciences and Engineering Division, Argonne National Laboratory, Lemont, Illinois 60439, United States;* orcid.org/0000-0002-6114-5524

Complete contact information is available at: https://pubs.acs.org/10.1021/acs.jpclett.4c02410

Notes

The authors declare no competing financial interest.

ACKNOWLEDGMENTS

This work was supported by the U.S. Department of Energy, Office of Science, Office of Basic Energy Sciences, Division of Chemical Sciences, Geosciences, and Biosciences at Argonne National Laboratory under contract no. DE-AC02-06CH11357. Specifically, this work was supported by Computational Chemical Sciences Program, under Award DE-SC0023382 funded by the U.S. Department of Energy, Office of Basic Energy Sciences, Chemical Sciences, Geosciences, and Biosciences Division. This work was completed in part with computing resources provided by the University of Chicago's Research Computing Center (RCC), Laboratory Computing Research Center (LCRC) at Argonne National Laboratory, and the National Energy Research Scientific Computing Center (NERSC) with award number BES-ERCAP0027337.

REFERENCES

(1) Nelson, R. C.; Miller, J. T. An introduction to X-ray absorption spectroscopy and its in situ application to organometallic compounds and homogeneous catalysts. *Catal. Sci. Technol.* **2012**, *2*, 461−470.

(2) Baker, M. L.; Mara, M. W.; Yan, J. J.; Hodgson, K. O.; Hedman, B.; Solomon, E. I. K- and L-edge X-ray absorption spectroscopy (XAS) and resonant inelastic X-ray scattering (RIXS) determination of differential orbital covalency (DOC) of transition metal sites. *Coord. Chem. Rev.* **2017**, *345*, 182−208.

(3) Chen, Z.; Walsh, A. G.; Zhang, P. Structural analysis of single-atom catalysts by X-ray absorption spectroscopy. *Acc. Chem. Res.* **2024**, *57*, 521−532.

(4) Resasco, J.; DeRita, L.; Dai, S.; Chada, J. P.; Xu, M.; Yan, X.; Finzel, J.; Hanukovich, S.; Hoffman, A. S.; Graham, G. W.; Bare, S. R.; Pan, X.; Christopher, P. Uniformity is key in defining structure−function relationships for atomically dispersed metal catalysts: The case of Pt/CeO_2. *J. Am. Chem. Soc.* **2020**, *142*, 169−184.

(5) Fang, L.; Seifert, S.; Winans, R. E.; Li, T. Operando XAS/SAXS: Guiding design of single-atom and subnanocluster catalysts. *Small Methods* **2021**, *5*, 2001194.

(6) Hahn, J. E.; Scott, R. A.; Hodgson, K. O.; Doniach, S.; Desjardins, S. R.; Solomon, E. I. Observation of an electric quadrupole transition in the X-ray absorption spectrum of a Cu (II) complex. *Chem. Phys. Lett.* **1982**, *88*, 595−598.

(7) Glatzel, P.; Bergmann, U. High resolution 1s core hole X-ray spectroscopy in 3d transition metal complexes—electronic and structural information. *Coord. Chem. Rev.* **2005**, *249*, 65−95.

(8) Spanjers, C. S.; Guillo, P.; Tilley, T. D.; Janik, M. J.; Rioux, R. M. Identification of second shell coordination in transition metal species using theoretical XANES: Example of Ti−O−(C, Si, Ge) complexes. *J. Phys. Chem. A* **2017**, *121*, 162−167.

(9) Trummer, D.; Searles, K.; Algasov, A.; Guda, S. A.; Soldatov, A. V.; Ramanantoanina, H.; Safonova, O. V.; Guda, A. A.; Copéret, C. Deciphering the phillips catalyst by orbital analysis and supervised machine learning from Cr Pre-edge XANES of molecular libraries. *J. Am. Chem. Soc.* **2021**, *143*, 7326−7341.

(10) Tomson, N. C.; Williams, K. D.; Dai, X.; Sproules, S.; DeBeer, S.; Warren, T. H.; Wieghardt, K. Re-evaluating the Cu K pre-edge XAS transition in complexes with covalent metal−ligand interactions. *Chem. Sci.* **2015**, *6*, 2474−2487.

(11) van Leest, N. P.; Tepaske, M. A.; Oudsen, J.-P. H.; Venderbosch, B.; Rietdijk, N. R.; Siegler, M. A.; Tromp, M.; van der Vlugt, J. I.; de Bruin, B. Ligand redox noninnocence in $[Co^{III}(TAML)]^{0/-}$ complexes affects nitrene formation. *J. Am. Chem. Soc.* **2020**, *142*, 552−563.

(12) Scarborough, C. C.; Lancaster, K. M.; DeBeer, S.; Weyhermüller, T.; Sproules, S.; Wieghardt, K. Experimental fingerprints for redox-Active terpyridine in $[Cr(tpy)_2](PF_6)_n$ (n = 3−0), and the remarkable electronic structure of $[Cr(tpy)_2]^{1--}$. *Inorg. Chem.* **2012**, *51*, 3718−3732.

(13) Lukens, J. T.; DiMucci, I. M.; Kurogi, T.; Mindiola, D. J.; Lancaster, K. M. Scrutinizing metal−ligand covalency and redox non-innocence via nitrogen K-edge X-ray absorption spectroscopy. *Chem. Sci.* **2019**, *10*, 5044−5055.

(14) Lyaskovskyy, V.; de Bruin, B. Redox non-innocent ligands: Versatile new tools to control catalytic reactions. *ACS Catal.* **2012**, *2*, 270−279.

(15) Féo, M.; Bakas, N. J.; Radović, A.; Parisot, W.; Clisson, A.; Chamoreau, L.-M.; Haddad, M.; Ratovelomanana-Vidal, V.; Neidig, M. L.; Lefèvre, G. Thermally stable redox noninnocent bathocuproine-iron complex for cycloaddition reactions. *ACS Catal.* **2023**, *13*, 4882−4893.

(16) Rickmeyer, K.; Niederegger, L.; Keilwerth, M.; Hess, C. R. Multifaceted role of the noninnocent mabiq ligand in promoting selective reduction of CO_2 to CO. *ACS Catal.* **2022**, *12*, 3046−3057.

(17) Xu, J.; Patel, P.; Kropf, A. J.; Kaphan, D.; Delferro, M.; Liu, C. Theoretical investigation of the hydrogenation of cyclohexene catalyzed by supported single-atom sites on redox noninnocent $LiMn_2O_4$ and $Li_2Mn_2O_4$ Surfaces. *J. Phys. Chem. C* **2024**, *128*, 4946−4957.

(18) Ghosh, A. Electronic structure of corrole derivatives: Insights from molecular structures, spectroscopy, electrochemistry, and quantum chemical calculations. *Chem. Rev.* **2017**, *117*, 3798−3881.

(19) Ganguly, S.; Ghosh, A. Seven clues to ligand noninnocence: The metallocorrole paradigm. *Acc. Chem. Res.* **2019**, *52*, 2003−2014.

(20) Vaillard, V. A.; Nieres, P. D.; Vaillard, S. E.; Doctorovich, F.; Sarkar, B.; Neuman, N. I. Cobalt, iron, and manganese metallocorroles in catalytic oxidation of water. An overview of the synthesis, selected redox and electronic properties, and catalytic activities. *Eur. J. Inorg. Chem.* **2022**, *2022*, No. e202100767.

(21) Nagaprasad Reddy, S.; Krishnamurthy, C. B.; Grinberg, I. First-principles study of the ligand substituent effect on ORR catalysis by metallocorroles. *J. Phys. Chem. C* **2020**, *124*, 11275−11283.

(22) Lei, H.; Li, X.; Meng, J.; Zheng, H.; Zhang, W.; Cao, R. Structure effects of metal corroles on energy-related small molecule activation reactions. *ACS Catal.* **2019**, *9*, 4320−4344.

(23) Levy, N.; Mahammed, A.; Kosa, M.; Major, D. T.; Gross, Z.; Elbaz, L. Metallocorroles as nonprecious-metal catalysts for oxygen reduction. *Angew. Chem., Int. Ed.* **2015**, *54*, 14080−14084.

(24) Ganguly, S.; Giles, L. J.; Thomas, K. E.; Sarangi, R.; Ghosh, A. Ligand noninnocence in iron corroles: Insights from optical and X-ray absorption spectroscopies and electrochemical redox potentials. *Chem.—Eur. J.* **2017**, *23*, 15098−15106.
(25) Ganguly, S.; Renz, D.; Giles, L. J.; Gagnon, K. J.; McCormick, L. J.; Conradie, J.; Sarangi, R.; Ghosh, A. Cobalt-and rhodium-corrole-triphenylphosphine complexes revisited: The question of a non-innocent corrole. *Inorg. Chem.* **2017**, *56*, 14788−14800.
(26) Ganguly, S.; McCormick, L. J.; Conradie, J.; Gagnon, K. J.; Sarangi, R.; Ghosh, A. Electronic structure of manganese corroles revisited: X-ray structures, optical and X-ray absorption spectroscopies, and electrochemistry as probes of ligand noninnocence. *Inorg. Chem.* **2018**, *57*, 9656−9669.
(27) Lim, H.; Thomas, K. E.; Hedman, B.; Hodgson, K. O.; Ghosh, A.; Solomon, E. I. X-ray absorption spectroscopy as a probe of ligand noninnocence in metallocorroles: The case of copper corroles. *Inorg. Chem.* **2019**, *58*, 6722−6730.
(28) Sarangi, R.; Giles, L. J.; Thomas, K. E.; Ghosh, A. Ligand noninnocence in silver corroles: A XANES investigation. *Eur. J. Inorg. Chem.* **2016**, *2016*, 3225−3227.
(29) Besley, N. A.; Gilbert, A. T.; Gill, P. M. Self-consistent-field calculations of core excited states. *J. Chem. Phys.* **2009**, *130*, 124308.
(30) Benzi, F.; Giuli, G.; Della Longa, S.; Paris, E. Vanadium *K*-edge XANES in vanadium-bearing model compounds: a full multiple scattering study. *J. Synchrotron Radiat.* **2016**, *23*, 947−952.
(31) DeBeer George, S.; Petrenko, T.; Neese, F. Prediction of iron K-edge absorption spectra using time-dependent density functional theory. *J. Phys. Chem. A* **2008**, *112*, 12936−12943.
(32) Jaszewski, A. R.; Stranger, R.; Pace, R. J. Time-dependent DFT studies of metal core-electron excitations in Mn complexes. *J. Phys. Chem. A* **2008**, *112*, 11223−11234.
(33) Cabaret, D.; Bordage, A.; Juhin, A.; Arfaoui, M.; Gaudry, E. First-principles calculations of X-ray absorption spectra at the K-edge of 3d transition metals: an electronic structure analysis of the pre-edge. *Phys. Chem. Chem. Phys.* **2010**, *12*, 5619−5633.
(34) Roemelt, M.; Beckwith, M. A.; Duboc, C.; Collomb, M.-N.; Neese, F.; DeBeer, S. Manganese K-edge X-ray absorption spectroscopy as a probe of the metal−ligand interactions in coordination compounds. *Inorg. Chem.* **2012**, *51*, 680−687.
(35) Krewald, V.; Lassalle-Kaiser, B.; Boron, T. T. I.; Pollock, C. J.; Kern, J.; Beckwith, M. A.; Yachandra, V. K.; Pecoraro, V. L.; Yano, J.; Neese, F.; DeBeer, S. The protonation states of oxo-bridged MnIV dimers resolved by experimental and computational Mn K pre-edge X-ray absorption spectroscopy. *Inorg. Chem.* **2013**, *52*, 12904−12914.
(36) Lee, K.; Wei, H.; Blake, A. V.; Donahue, C. M.; Keith, J. M.; Daly, S. R. Ligand K-edge XAS, DFT, and TDDFT analysis of pincer linker variations in Rh(i) PNP complexes: reactivity insights from electronic structure. *Dalton Trans.* **2016**, *45*, 9774−9785.
(37) Nascimento, D. R.; Govind, N. Computational approaches for XANES, VtC-XES, and RIXS using linear-response time-dependent density functional theory based methods. *Phys. Chem. Chem. Phys.* **2022**, *24*, 14680−14691.
(38) Patel, P.; Lu, Z.; Jafari, M. G.; Hernández-Prieto, C.; Zatsepin, P.; Mindiola, D. J.; Kaphan, D. M.; Delferro, M.; Kropf, A. J.; Liu, C. Integrated experimental and computational K-edge X-ray absorption near-edge structure analysis of vanadium catalysts. *J. Phys. Chem. C* **2022**, *126*, 11949−11962.
(39) Vidal, M. L.; Feng, X.; Epifanovsky, E.; Krylov, A. I.; Coriani, S. New and efficient equation-of-motion coupled-cluster framework for core-excited and core-ionized states. *J. Chem. Theory Comput.* **2019**, *15*, 3117−3133.
(40) Park, Y. C.; Perera, A.; Bartlett, R. J. Equation of motion coupled-cluster study of core excitation spectra II: Beyond the dipole approximation. *J. Chem. Phys.* **2021**, *155*, 094103.
(41) Ray, K.; DeBeer George, S.; Solomon, E. I.; Wieghardt, K.; Neese, F. Description of the ground-state covalencies of the bis (Dithiolato) transition-metal complexes from X-ray absorption spectroscopy and time-dependent density-functional calculations. *Chem.—Eur. J.* **2007**, *13*, 2783−2797.
(42) Buenker, R. J.; Peyerimhoff, S. D. Individualized configuration selection in CI calculations with subsequent energy extrapolation. *Theor. Chim. Acta* **1974**, *35*, 33−58.
(43) Buenker, R. J.; Peyerimhoff, S. D. Energy extrapolation in CI calculations. *Theor. Chim. Acta* **1975**, *39*, 217−228.
(44) Mahapatra, U. S.; Datta, B.; Mukherjee, D. A state-specific multi-reference coupled cluster formalism with molecular applications. *Mol. Phys.* **1998**, *94*, 157−171.
(45) Malmqvist, P. Å.; Rendell, A.; Roos, B. O. The restricted active space self-consistent-field method, implemented with a split graph unitary group approach. *J. Phys. Chem.* **1990**, *94*, 5477−5482.
(46) Malmqvist, P. Å.; Pierloot, K.; Shahi, A. R. M.; Cramer, C. J.; Gagliardi, L. The restricted active space followed by second-order perturbation theory method: Theory and application to the study of CuO2 and Cu2O2 systems. *J. Chem. Phys.* **2008**, *128*, 204109.
(47) Guo, M.; Sørensen, L. K.; Delcey, M. G.; Pinjari, R. V.; Lundberg, M. Simulations of iron K pre-edge X-ray absorption spectra using the restricted active space method. *Phys. Chem. Chem. Phys.* **2016**, *18*, 3250−3259.
(48) Li Manni, G.; Carlson, R. K.; Luo, S.; Ma, D.; Olsen, J.; Truhlar, D. G.; Gagliardi, L. Multiconfiguration pair-density functional theory. *J. Chem. Theory Comput.* **2014**, *10*, 3669−3680.
(49) Ghosh, S.; Mukamel, S.; Govind, N. A combined wave function and density functional approach for K-edge X-ray absorption near-edge spectroscopy: A case study of hydrated first-row transition metal ions. *J. Phys. Chem. Lett.* **2023**, *14*, 5203−5209.
(50) Ghosh, S.; Agarwal, H.; Galib, M.; Tran, B.; Balasubramanian, M.; Singh, N.; Fulton, J. L.; Govind, N. Near-quantitative predictions of the first-shell coordination structure of hydrated first-row transition metal ions using K-edge X-ray absorption near-edge spectroscopy. *J. Phys. Chem. Lett.* **2022**, *13*, 6323−6330.
(51) Roos, B. O.; Veryazov, V.; Conradie, J.; Taylor, P. R.; Ghosh, A. Not innocent: Verdict from ab initio multiconfigurational second-order perturbation theory on the electronic structure of chloroiron corrole. *J. Phys. Chem. B* **2008**, *112*, 14099−14102.
(52) Phung, Q. M.; Muchammad, Y.; Yanai, T.; Ghosh, A. A DMRG/CASPT2 investigation of metallocorroles: Quantifying ligand noninnocence in archetypal 3d and 4d element derivatives. *JACS Au* **2021**, *1*, 2303−2314.
(53) Pierloot, K.; Phung, Q. M.; Ghosh, A. Electronic structure of neutral and anionic iron−nitrosyl corrole. A multiconfigurational and density matrix renormalization group investigation. *Inorg. Chem.* **2020**, *59*, 11493−11502.
(54) Halbert, L.; Vidal, M. L.; Shee, A.; Coriani, S.; Severo Pereira Gomes, A. Relativistic EOM-CCSD for Core-Excited and Core-Ionized State Energies Based on the Four-Component Dirac−Coulomb (- Gaunt) Hamiltonian. *J. Chem. Theory Comput.* **2021**, *17*, 3583−3598.
(55) Zakharieva, O.; Schünemann, V.; Gerdan, M.; Licoccia, S.; Cai, S.; Walker, F. A.; Trautwein, A. X. Is the corrolate macrocycle innocent or noninnocent? Magnetic susceptibility, mössbauer, 1H NMR, and DFT investigations of chloro- and phenyliron corrolates. *J. Am. Chem. Soc.* **2002**, *124*, 6636−6648.
(56) Nardis, S.; Cicero, D. O.; Licoccia, S.; Pomarico, G.; Berionni Berna, B.; Sette, M.; Ricciardi, G.; Rosa, A.; Fronczek, F. R.; Smith, K. M.; Paolesse, R. Phenyl derivative of iron 5,10,15-tritolylcorrole. *Inorg. Chem.* **2014**, *53*, 4215−4227.
(57) Bhowmick, R.; Roy Chowdhury, S.; Vlaisavljevich, B. Molecular geometry and electronic structure of copper corroles. *Inorg. Chem.* **2023**, *62*, 13877−13891.
(58) Polly, R.; Schacherl, B.; Rothe, J.; Vitova, T. Relativistic Multiconfigurational Ab Initio Calculation of Uranyl 3d4f Resonant Inelastic X-ray Scattering. *Inorg. Chem.* **2021**, *60*, 18764−18776.
(59) Sergentu, D.-C.; Duignan, T. J.; Autschbach, J. Ab Initio Study of Covalency in the Ground versus Core-Excited States and X-ray Absorption Spectra of Actinide Complexes. *J. Phys. Chem. Lett.* **2018**, *9*, 5583−5591.
(60) Becke, A. D. A new mixing of Hartree−Fock and local density-functional theories. *J. Chem. Phys.* **1993**, *98*, 1372−1377.

https://doi.org/10.1021/acs.jpclett.4c02410
J. Phys. Chem. Lett. XXXX, XXX, XXX−XXX

(61) Weigend, F.; Ahlrichs, R. Balanced basis sets of split valence, triple zeta valence and quadruple zeta valence quality for H to Rn: Design and assessment of accuracy. *Phys. Chem. Chem. Phys.* **2005**, *7*, 3297−3305.
(62) Stoychev, G. L.; Auer, A. A.; Neese, F. Automatic generation of auxiliary basis sets. *J. Chem. Theory Comput.* **2017**, *13*, 554−562.
(63) Neese, F.; Wennmohs, F.; Hansen, A.; Becker, U. Efficient, approximate and parallel Hartree−Fock and hybrid DFT calculations. A 'chain-of-spheres' algorithm for the Hartree−Fock exchange. *Chem. Phys.* **2009**, *356*, 98−109.
(64) Adamo, C.; Barone, V. Toward reliable density functional methods without adjustable parameters: The PBE0 model. *J. Chem. Phys.* **1999**, *110*, 6158−6170.
(65) Pantazis, D. A.; Chen, X.-Y.; Landis, C. R.; Neese, F. All-electron scalar relativistic basis sets for third-row transition metal atoms. *J. Chem. Theory Comput.* **2008**, *4*, 908−919.
(66) Neese, F. Software update: The ORCA program system—Version 5.0. *Wiley Interdiscip. Rev. Comput. Mol. Sci.* **2022**, *12*, No. e1606.
(67) Malmqvist, P.-Å.; Roos, B. O. The CASSCF state interaction method. *Chem. Phys. Lett.* **1989**, *155*, 189−194.
(68) Aquilante, F.; Autschbach, J.; Baiardi, A.; Battaglia, S.; Borin, V. A.; Chibotaru, L. F.; Conti, I.; De Vico, L.; Delcey, M.; Ferré, N.; et al. Modern quantum chemistry with [Open] Molcas. *J. Chem. Phys.* **2020**, *152*, 214117.
(69) Roos, B. O.; Lindh, R.; Malmqvist, P.-Å.; Veryazov, V.; Widmark, P.-O. New relativistic ANO basis sets for transition metal atoms. *J. Phys. Chem. A* **2005**, *109*, 6575−6579.

https://doi.org/10.1021/acs.jpclett.4c02410
J. Phys. Chem. Lett. XXXX, XXX, XXX−XXX